NISTIR 6370

Benchmark Experimental Database for Multiphase Combustion Model Input and Validation: Characterization of the Inlet Combustion Air

John F. Widmann
S. Rao Charagundla
Cary Presser
Process Measurements Division
Chemical Science and Technology Laboratory
U. S. Department of Commerce
National Institute of Standards and Technology
Gaithersburg, Maryland 20899

July 1999

Contents

page

1. Introduction 1

2. Numerical Methodology 3

3. Experimental 5

4. Results and Discussion 8

5. Conclusions 17

6. Acknowledgements 17

7. References 18

Notation

B	vane height
$C_{1\varepsilon}$, $C_{2\varepsilon}$, C_{μ}	constants in turbulence model equations
D_0	inner diameter of the outer pipe of the annular regions
D_i	outer diameter of the inner pipe of the annular regions
F_i	body forces
G_k	generation of k due to turbulent stresses
G_b	generation of k due to buoyancy
G_{θ}	axial flux of angular momentum
G_z	axial flux of axial momentum
k	turbulent kinetic energy
L	characteristic length
n_v	number of vanes
p	static pressure
p_0	total pressure
p_n	static pressure at location n
Pr_t	turbulent Prandtl number
r	radial coordinate
R_0	radial location of the outer wall of the annular passages
Re	Reynolds number
R_i	radial location of the inner wall of the annular passages
R_v	distance from the burner axis to the vanes
S	swirl number
t	time
T	temperature
u, $\overline{u}$	mean velocity
u_i, u_j, u_k	velocity components in Cartesian coordinates
u_{θ}	tangential velocity component
u_z	axial velocity component
$\overline{u}_z$	mean axial velocity based upon the volumetric flow rate
x_i, x_j, x_k	Cartesian coordinates
z	axial coordinate

Greek letters

α	vane angle defined in Fig. 2B
α'	vane angle defined by Beér and Chigier (1974)
B	coefficient of thermal expansion
X	blockage factor
δ_{ij}	Kronecker delta
ε	turbulence dissipation rate
ν	kinematic viscosity
λ	vane thickness
μ	viscosity
μ_t	eddy or turbulent viscosity

θ	polar angle
ρ	density
σ	ratio of the average tangential and radial velocity components
σ_k, σ_ε	constants in the turbulence model equations
Ψ	alignment parameter

Benchmark Experimental Database for Multiphase Combustion Model Input and Validation: Characterization of the Inlet Combustion Air

John F. Widmann, S. Rao Charagundla, and Cary Presser
Chemical Science and Technology Laboratory
National Institute of Standards and Technology
100 Bureau Drive, Stop 8360
Gaithersburg, MD 20899-8360, USA

Abstract

The air flow through a vane-cascade swirl generator is examined both experimentally and numerically to characterize the inlet combustion air flow entering a reference spray combustion facility at NIST. A three-dimensional model is used to simulate the aerodynamics in the 12-vane cascade swirl generator that imparts the desired degree of angular momentum to the air in the annulus leading into the reactor. A numerical simulation using the Renormalization Group method (RNG) k-ε turbulence model results in a velocity profile consistent with experimental measurements, and correctly predicts a recirculation zone that is experimentally observed at the exit of the annular passage. The standard k-ε turbulence model does not compare as well with the experimental data and fails to predict the recirculation zone at the exit. This work is part of a larger project at NIST in which benchmark data are collected for input and validation of multiphase combustion models, and the results presented provide a well-characterized inlet condition for the spray combustion reactor[†]. The good agreement between the experimental data and the simulation with the RNG k-ε turbulence model provides further validation for this model in confined, annular flows.

Keywords: Swirl, Turbulence, Fluid Mechanics, Numerical Analysis, Simulation, CFD, Pitot Probe

1. Introduction

The design and optimization of multiphase thermal oxidation systems in the power generation, waste incineration, and chemical process industries are relying increasingly on computational models and simulations to provide relevant process information in a cost-effective manner. System performance is dependent on the liquid atomization, chemistry, aerodynamic design, and the degree of liquid/air mixing within the reactor. In general, there is a need for experimental data detailing the characteristics of the droplet field and flame structure, and an understanding of their interrelationship with the system operating conditions, for the development and validation of advanced computational models. This paper is part of a larger effort at the National Institute of Standards and Technology (NIST) to provide benchmark data that can be used for input and validation of multiphase combustion models and submodels.

The experimental facility consists of an enclosed spray combustion reactor and is shown schematically in Fig. 1. The combustion air passes through a 12-vane swirl

---

[†] Electronic files of the data presented in this report are available. Contact Cary Presser at *cpresser@nist.gov*.

cascade, shown in Fig. 1A, that imparts the angular momentum necessary to stabilize the flame, and flows around the nozzle before entering the reactor. The vane angle and air flow rate are 50^{o} and 0.0158 $m^3\ s^{-1}$, respectively, and correspond to the baseline case of the NIST database (Widmann *et al.*, 1999). For the reported air flow rate, the Reynolds number, $Re = (D_0 - D_i)\overline{u_z}/\nu$, in the annular region of the swirl generator is equal to 1.0 x 10^4. Note that the radial locations of the inner and outer walls of the annular passage downstream of the swirl vanes are shown in the figure (R_i = 0.0175 m and R_0 = 0.0508 m, respectively).

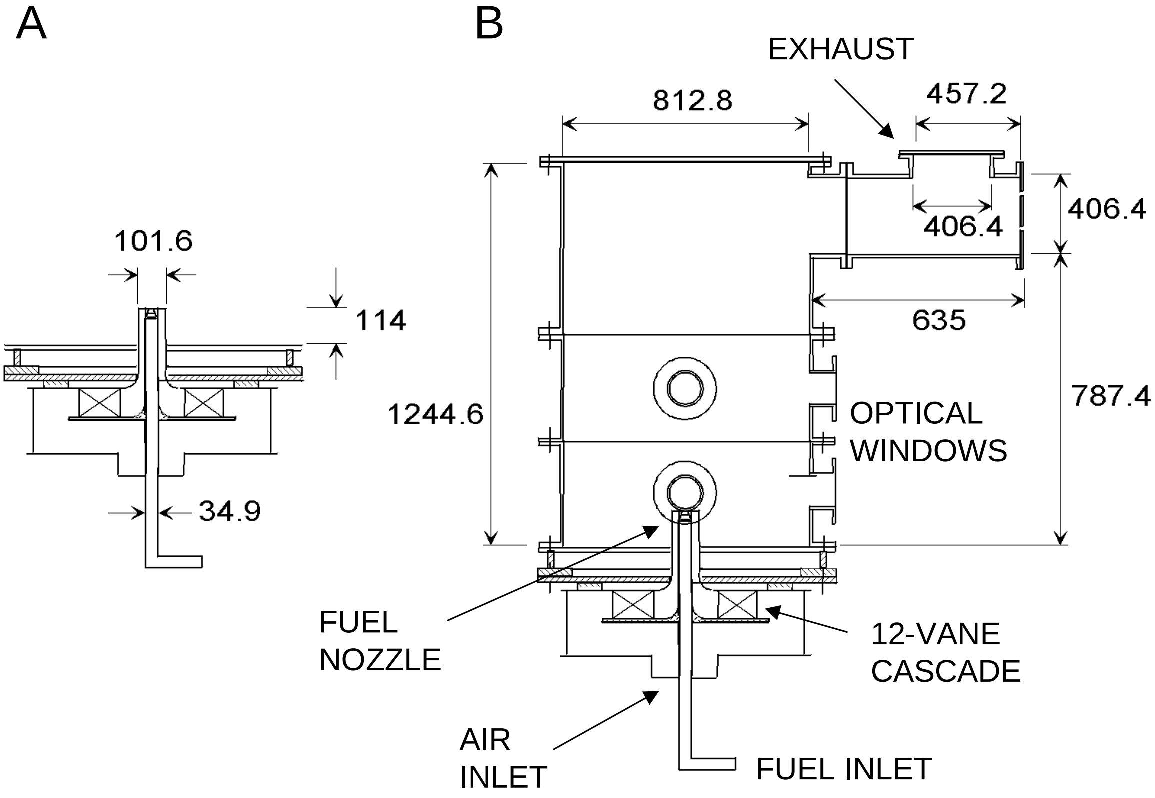

Fig. 1 Schematic of (A) the 12-vane cascade swirl generator and (B) the spray combustion reactor. Dimensions are given in millimeters.

In this paper, the airflow through the vane cascade swirl generator shown in Fig. 1A was simulated using FLUENT† computational fluid dynamics software (FLUENT Inc., 1998), and results obtained using two turbulence models are presented and compared to experimental data. The two turbulence models, the standard k-ε model (Launder and Spalding, 1972) and the Renormalized Group theory (RNG) k-ε model (Yakhot and Orszag, 1986), are two equation models in which scalar quantities (the turbulent kinetic

---

† Certain commercial equipment, materials, or software are identified in this publication to specify adequately the experimental procedure. Such identification does not imply recommendation or endorsement by the National Institute of Standards and Technology, nor does it imply that the materials or equipment are necessarily the best available for this purpose.

energy, *k*, and its dissipation rate, *ε*) are used to describe the production, diffusion, and dissipation of turbulence.

The standard *k-ε* model is a semi-empirical turbulence model based upon an isotropic eddy-viscosity hypothesis. It is widely used in industrial flow and heat transfer simulations due to its robustness, economy, and reasonable accuracy (Shyy *et al.*, 1997). The RNG *k-ε* model also belongs to the *k-ε* family of turbulence models; however, unlike the standard *k-ε* model, the RNG *k-ε* model was derived using a statistical technique called renormalization group methods. The model equations are similar to the standard *k-ε* model, but the statistical derivation results in different values for the various constants in the equations.

Smith and Reynolds (1992), however, reported problems with the specific values of the constants in the RNG *k-ε* model. In response, Yakhot and coworkers reformulated the earlier derivation of the differential equation describing the transport of *ε* (Yakhot *et al.*, 1992; Yakhot and Smith, 1992). With this change, the RNG *k-ε* turbulence model has shown improvement over the standard *k-ε* model when applied to many industrial flows (e.g., Papageorgakis and Assanis, 1999; Yin *et al.*, 1996; Lien and Leschziner, 1994; Yakhot *et al.*, 1992). Particularly noteworthy is the rate-of-strain term in the transport equation for *ε* that has been reported to result in improved predictions of flow fields with high strain rates. In particular, flows in curved geometries, stagnation flows, separated flows, and swirling flows are situations in which the RNG *k-ε* model has been reported to be more accurate than the standard *k-ε* turbulence model. Benim (1990) compared the performance of these two turbulence models in a swirling combustor and found that the RNG *k-ε* model resulted in predictions consistent with experiment, while the standard *k-ε* model compared poorly with the experimental data. In this study, we apply both of these models to simulations of flow through a vane cascade swirl generator, including the swirling flow through the annulus following the vanes. Jaw and Chen (1998) recently reviewed second-order closure turbulence models, and the reader is referred there for a more detailed discussion of these and other turbulence models.

2. Numerical Methodology

The numerical formulation is for isothermal, turbulent airflow through the 12-vane cascade swirl generator shown in Fig. 1A. The relevant conservation equations include continuity, the Reynold's averaged Navier-Stokes equations, and an appropriate turbulence model. The Reynolds averaged Navier-Stokes equations are generated from the instantaneous Navier-Stokes equations using the following transformations (Bird *et al.*, 1960):

$$u_i = \bar{u}_i + u'_i \,, \quad \rho = \bar{\rho} + \rho' \,, \ \text{and} \quad p = \bar{p} + p' \,. \tag{1}$$

Here, the overbar and prime indicate a time-averaged quantity and an instantaneous fluctuation, respectively. Dropping the overbar for convenience, the resulting expression for the momentum equation in cartesian coordinates is

$$\frac{\partial}{\partial t}(\rho u_i) + \frac{\partial}{\partial x_j}(\rho u_i u_j) = -\frac{\partial p}{\partial x_i} + \frac{\partial}{\partial x_j}\left[\mu\left(\frac{\partial u_i}{\partial x_j} + \frac{\partial u_j}{\partial x_i}\right) - \frac{2}{3}\mu\frac{\partial u_k}{\partial x_k}\delta_{ij}\right] + F_i + \frac{\partial}{\partial x_j}(-\rho\overline{u'_i u'_j}) \,. \tag{2}$$

The last term in Eq. (2) is the derivative of the *Reynolds stresses,* $-\rho\overline{u_i' u_j'}$, and represents the effect of turbulence on the momentum balance. The Reynolds stresses represent additional unknowns, and a set of constitutive equations is required to close these equations. The turbulence models provide the additional equations necessary to close the transport equations.

The Reynolds stresses in Eq. (2) are computed using the Boussinesq hypothesis (Hinze, 1975),

$$-\rho\overline{u_i u_j} = \mu_t\left(\frac{\partial u_i}{\partial x_j}+\frac{\partial u_j}{\partial x_i}\right)-\frac{2}{3}\left(\rho k+\mu_t\frac{\partial u_i}{\partial x_i}\right)\delta_{ij}\ , \tag{3}$$

where μ_t is the *eddy* or *turbulent viscosity* computed from

$$\mu_t = \rho C_\mu \frac{k^2}{\varepsilon}\ . \tag{4}$$

For the standard k-ε turbulence model, the scalar quantities k and ε are computed from the following transport equations:

$$\frac{\partial}{\partial t}(\rho k)+\frac{\partial}{\partial x_i}(\rho u_i k)=\frac{\partial}{\partial x_i}\left[\left(\mu+\frac{\mu_t}{\sigma_k}\right)\frac{\partial k}{\partial x_i}\right]+G_k+G_b-\rho\varepsilon \tag{5}$$

and

$$\frac{\partial}{\partial t}(\rho\varepsilon)+\frac{\partial}{\partial x_i}(\rho u_i\varepsilon)=\frac{\partial}{\partial x_i}\left[\left(\mu+\frac{\mu_t}{\sigma_k}\right)\frac{\partial\varepsilon}{\partial x_i}\right]+C_{1\varepsilon}\frac{\varepsilon}{k}\{G_k+(1-C_{3\varepsilon})G_b\}-C_{2\varepsilon}\rho\frac{\varepsilon^2}{k}\ . \tag{6}$$

The generation of k due to turbulent stresses, G_k, and the generation of k due to buoyancy, G_b, are given by

$$G_k = -\rho\overline{u_i u_j}\frac{\partial u_j}{\partial x_i} \tag{7}$$

and

$$G_b = -\beta g_i\frac{u_t}{\mathrm{Pr}_t}\frac{\partial T}{\partial x_i}\ , \tag{8}$$

respectively. Here, Pr_t is the turbulent Prandtl number (Kreith, 1958), and β is the coefficient of thermal expansion. For these simulations, the flow is assumed to be isothermal and Eq. (8) is neglected. The values of the constants in Eqs. (4) - (6) have been determined experimentally to be $C_{1\varepsilon}$ = 1.44, $C_{2\varepsilon}$ = 1.92, C_μ = 0.09, σ_k = 1.0, σ_e = 1.3, and Pr_t = 0.85 (Launder and Spalding, 1972).

The numerical simulations were generated using a segregated, implicit solver. Integrating the transient problem to steady state was found to be computationally less expensive than solving the time-independent transport equations, and this method was used for the results presented here. The coupled equations were solved with first order accuracy in time and second order accuracy in momentum, continuity, and turbulence parameters. The pressure and velocity were coupled using the PISO algorithm (Issa,

1986) with neighbor and skewness correction, and standard wall functions (Launder and Spalding, 1974) were used for the near-wall treatment.

A uniform velocity profile with a magnitude of 2.2 m s^{-1} was used for the inlet condition, and an inlet turbulence intensity of 10 % was assumed with a characteristic length of $R_0 - R_i = 0.0333$ m. The predictions at the outlet of the domain were not found to be sensitive to the inlet turbulence intensity. For the conditions considered, the Reynolds number based upon the mean axial velocity is 1.0×10^4 in the annular regions of the domain. Sheen *et al*. (1997) reported the transition from laminar to turbulent flow to occur at Re = 1600; therefore, we expect fully developed turbulent flow here. At the outlet, the radial velocity was assumed to be negligible and the radial equilibrium pressure distribution was calculated by

$$\frac{\partial p}{\partial r} = \frac{\rho u_\theta^2}{r}. \tag{9}$$

Also at the outlet, the turbulence intensity and characteristic length used for the inlet condition were assumed in the event of backflow into the domain, such as in a recirculation zone.

The airflow through the 12-vane cascade swirl generator was simulated using FLUENT computational fluid dynamics software (FLUENT Inc., 1998). A three-dimensional model is required for this geometry; however, due to symmetry it is only necessary to simulate a 30° portion of the vane cascade. An unstructured grid was used for the simulations, and the surface mesh is shown in Fig. 2A. Note that the rotationally periodic symmetry planes at $\theta = 0^o$ and $\theta = 30^o$ are not shown in the figure. The mesh was constructed so that the grid resolution gradually increased from the inlet to the vanes, and then remained high throughout the remainder of the domain. The number of cells in the mesh was systematically increased until the solution was determined to be grid-independent, and this strategy of gradually increasing the resolution from the inlet plane to the vanes was used for all of the grids. The predictions presented here correspond to results obtained from a grid with approximately 277,000 cells. A top view of the vanes is shown in Fig. 2B, and the 30° section that was modeled is depicted. Note that the vane angle, α, is 50° and shown in the figure.

3. Experimental

The experimental facility consists of the enclosed spray combustion reactor shown in Fig. 1. In this facility, the combustion air passes through a 12-vane swirl cascade, shown in Fig. 1A, that imparts the angular momentum necessary to stabilize the flame, and flows around the nozzle before entering the reactor. The reactor consists of a stainless steel enclosure approximately 1.2 m in height and 0.8 m in diameter, and is shown in Fig. 1B. The vane angle and air flow rate are 50° and 0.0158 m^3 s^{-1}, respectively, and correspond to the baseline case of the NIST database (Widmann *et al*., 1999). For these experiments, the combined standard uncertainties in these measurements are ± 1° and ± 0.0005 m^3 s^{-1} for the vane angle and air flow rate, respectively. The air enters the reactor at ambient temperature and pressure. Additional details of the facility and the benchmark database program at NIST are available elsewhere (Widmann *et al*., 1999).

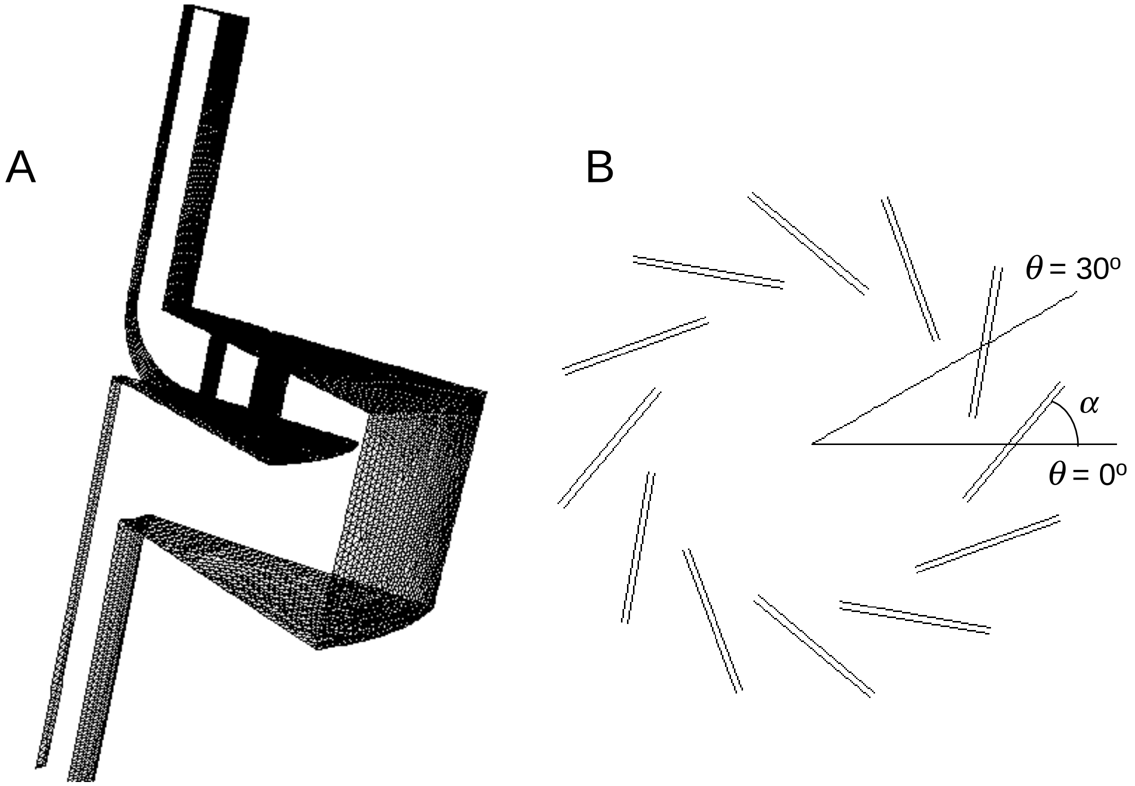

Fig. 2 Schematic of (A) the surface mesh used to generate the unstructured grid for the numerical simulation, and (B) a top view of the 12-vane cascade and the modeled 30^o section. Note that the periodic boundaries in (A) have been omitted for clarity.

The magnitude of the air velocity was measured at the outlet of the annulus following the vanes as a function of radial position to validate the simulations. A five-hole pitot probe with a hemispherical head was used for the velocity measurements. The probe has a cylindrical tip with a length of 26 mm and a diameter of 1.7 mm. Following the 26 mm tip, the diameter of the probe increases smoothly from 1.7 mm to 3.2 mm, which is the diameter of the main body of the probe. The probe has one hole on the head of the probe tip for total pressure measurements, and four holes located 13 mm from the head and 90^o apart on the side of the probe for static pressure measurements. The four velocity measurements corresponding to the four different static pressure holes were used to align the probe in the direction of the flow, and the average of the four measurements was reported as the mean velocity. The differential pressures were measured using Autotran pressure transducers (Model 750D-031) with measurement ranges of 0 Pa - 24.9 Pa and ± 12.5 Pa.

To calibrate the pitot probe, velocity measurements were obtained in a low velocity wind tunnel at NIST. Data are presented in Fig. 3 for four values of the probe angle, defined as the angle between the direction of the mean velocity vector and the probe, and the error bars correspond to the standard deviation of the four velocity measurements. A probe angle of 0^o indicates that the probe was aligned with the flow. The ordinate corresponds to the velocity magnitude calculated using Bernoulli's equation (Bird *et al.*, 1960),

$$u_n = \sqrt{\frac{2}{\rho}\left[p_0 - p_n\right]}, \tag{10}$$

where p_0 is the measured total pressure and p_n is the measured static pressure at the n^{th} hole. The measurements obtained using Eq. (10) are in very good agreement with the known velocity in the wind tunnel for probe angles less than 10^o, and are in fair agreement for larger probe angles. The velocity measurements reported in this paper were not computed using Eq. (10), but were determined from the calibration in Fig. 3.

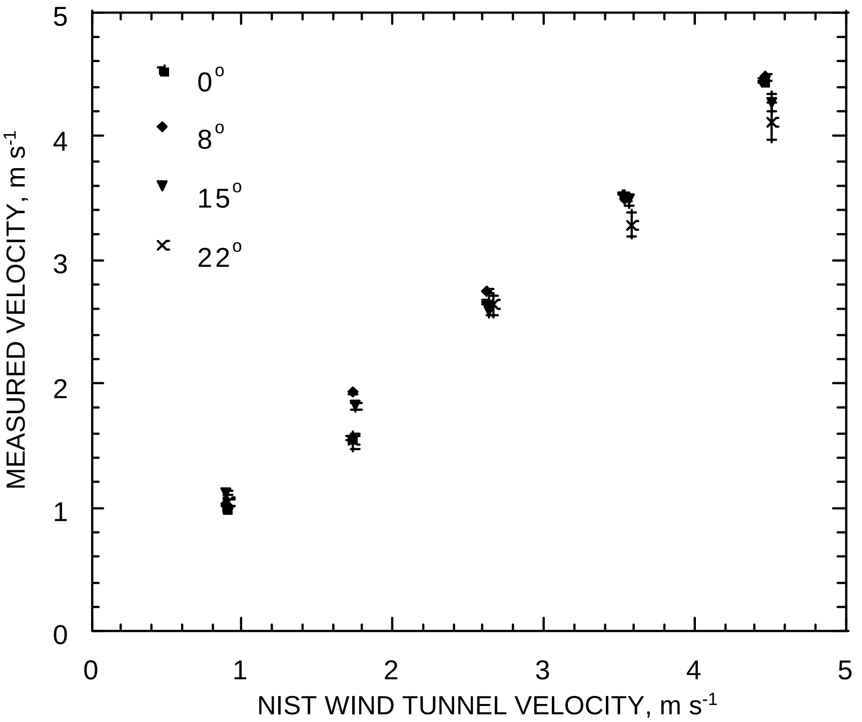

Fig. 3 Pitot probe calibration at four different probe angles.

To obtain accurate results, the pitot probe must be reasonably aligned with the mean direction of the flow. However, Fig. 3 reveals that some deviation in the alignment is acceptable and will not impact the measurements. For example, probe angles of 0^o and 8^o result in velocity measurements that agree within 2 % for $u > 3$ m s^{-1} in the calibration data. To facilitate aligning the pitot probe in the flow and quantifying the uncertainties in the measurements, a non-dimensional alignment parameter, Ψ, was used where Ψ is defined as

$$\Psi = \frac{1}{\overline{u}}\sqrt{\frac{1}{2}\left[(u_1 - u_3)^2 + (u_2 - u_4)^2\right]}. \qquad (11)$$

Here, $\overline{u}$ is the average of the four velocity measurements. The differences (u_1 - u_3) and (u_2 - u_4) in Eq. (11) correspond to the velocities computed from the static pressure holes that are 180° apart on the side of the pitot probe. The alignment parameter facilitates aligning the probe in the flow by utilizing the symmetry of the probe, and should not be confused with a "fractional error." However, Ψ was used to estimate the uncertainties in the measurements by comparing data obtained in the NIST wind tunnel with data obtained in the swirling flow. Figure 4 presents the calculated alignment parameter from the calibration data. Note that although Ψ increases with increasing probe angle as anticipated, it is below 0.07 for probe angles as large as 15°. For probe angles of 0° and 8°, Ψ is below 0.015 for $u > 1.5$ m s^{-1}.

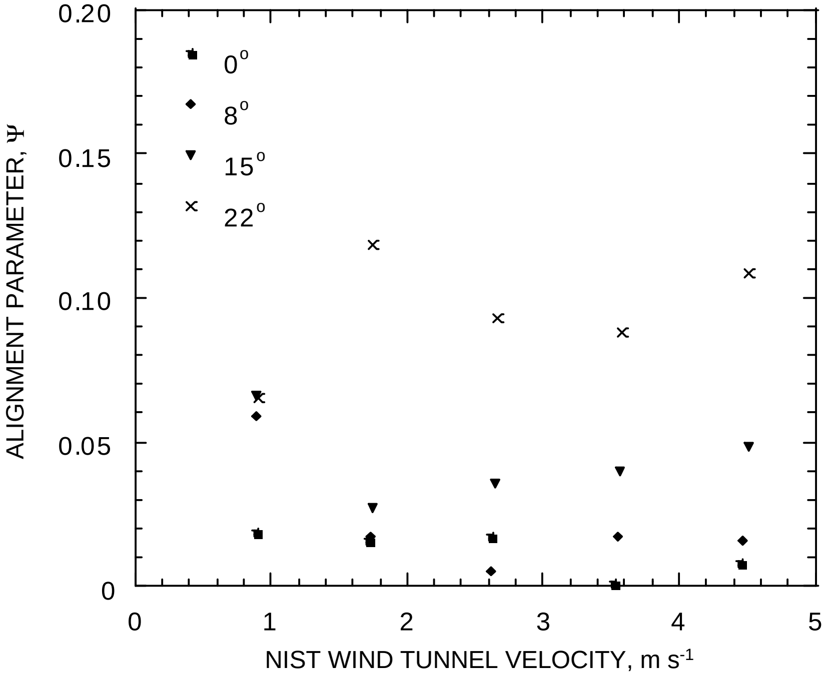

Fig. 4 Alignment parameter, Ψ, calculated from the pitot probe calibration in Fig. 3.

4. Results and Discussion

RNG k-ε vs. standard k-ε turbulence model

The combustion air enters at the bottom of the swirl generator with a uniform velocity profile and flows through an annular section approximately 0.178 m long with the same radial dimensions as the exit annulus (R_i = 0.0175 m and R_0 = 0.0508 m). The flow is then directed radially outward as shown in Fig. 1B. The flow bends upward and then returns toward the center of the swirl generator as it passes through the vanes. The swirling flow is directed upward, passes through an exit annulus approximately 0.165 m long and enters the reactor. The fuel nozzle is introduced into the reactor through the inner pipe of the annulus; therefore, the swirling combustion air flows around the nozzle as it enters the reactor.

The predictions of the magnitude of the air velocity through the vane-cascade swirl generator using the standard k-ε and the RNG k-ε turbulence models are presented in Fig. 5. The standard k-ε model predicts a maximum velocity in the annulus of $\approx$ 4.8 m s^{-1}, while the RNG k-ε model predicts a maximum velocity of $\approx$ 5.2 m s^{-1}. Both models predict that the air rapidly accelerates as it enters the annulus following the swirl vanes; however, the RNG k-ε model results in larger velocity gradients, with the high velocity regions of the flow being more localized. This behavior is also evident in the lower portion of the domain beneath the swirl vanes. The stagnation zone in the corner corresponding to the first bend as the flow leaves the lower annulus is larger for the RNG k-ε model, and all of the recirculation zones in the domain have higher total velocities. In comparison, the standard k-ε model results in flow field predictions in which the velocity field is smoother, resulting in lower peak velocities and lower velocity gradients.

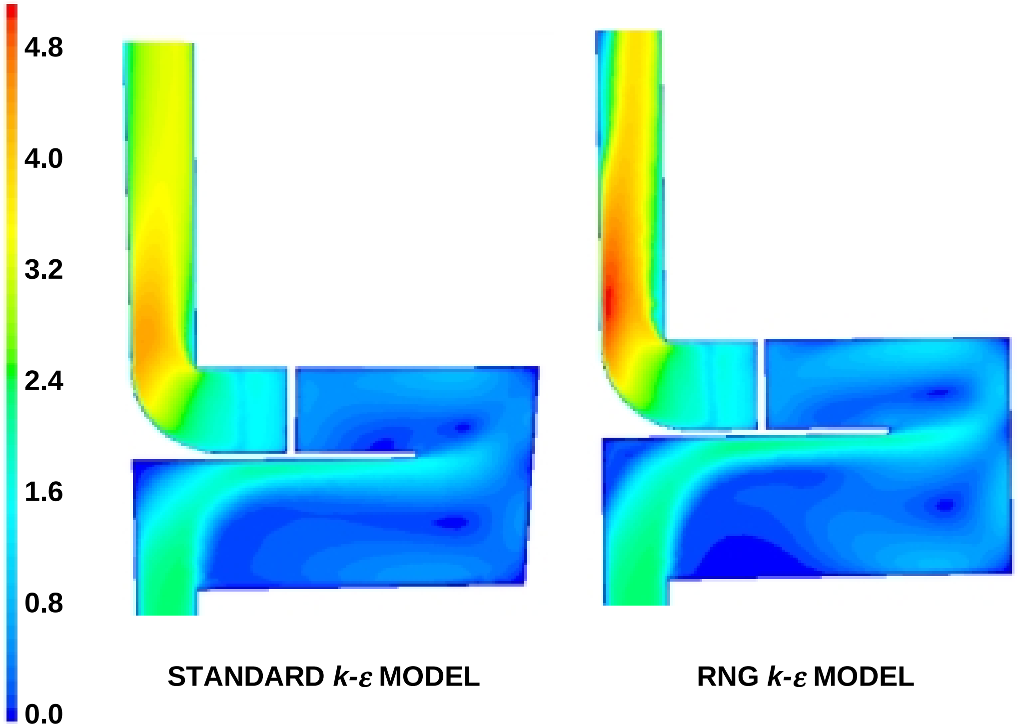

Fig. 5 Contour plots of the predicted magnitude of the velocity vector for the standard k-ε and RNG k-ε turbulence models. The contour plots correspond to the periodic boundaries at $\theta = 0^{\circ}$ and $\theta = 30^{\circ}$, and the scale ranges from 0 m s^{-1} to 5.2 m s^{-1} for both plots.

Contour plots showing the predicted turbulence intensity in the annulus following the swirl vanes for both models are shown in Fig. 6. Note that the two plots have different scales, with turbulence intensities in the range 0.2 - 0.8 and 0 - 0.6 for the standard k-ε model and the RNG k-ε model, respectively. The two turbulence models result in significantly different predictions for the turbulence intensity in this swirling flow field. Both models predict the generation of turbulence at the corner where the annulus intersects with the horizontal section of the swirl generator (lower right corner of the contour plots in Fig. 6). However, vortex shedding is noticeable in the prediction of the RNG k-ε model, while the standard k-ε model results in significantly more dispersion of turbulence. The standard k-ε model predicts a central core of turbulence in the annulus that decays with axial position. In contrast, the RNG k-ε model predicts significantly less turbulence in the central region of the annulus, with regions of high turbulence being primarily in the near-wall region of the inner wall and the vortex shedding near the corner of the outer wall. Further downstream within the annular passage, the flow separates from the inner wall due to the adverse pressure gradient that results from the swirling flow, and which in turn produces increased turbulence.

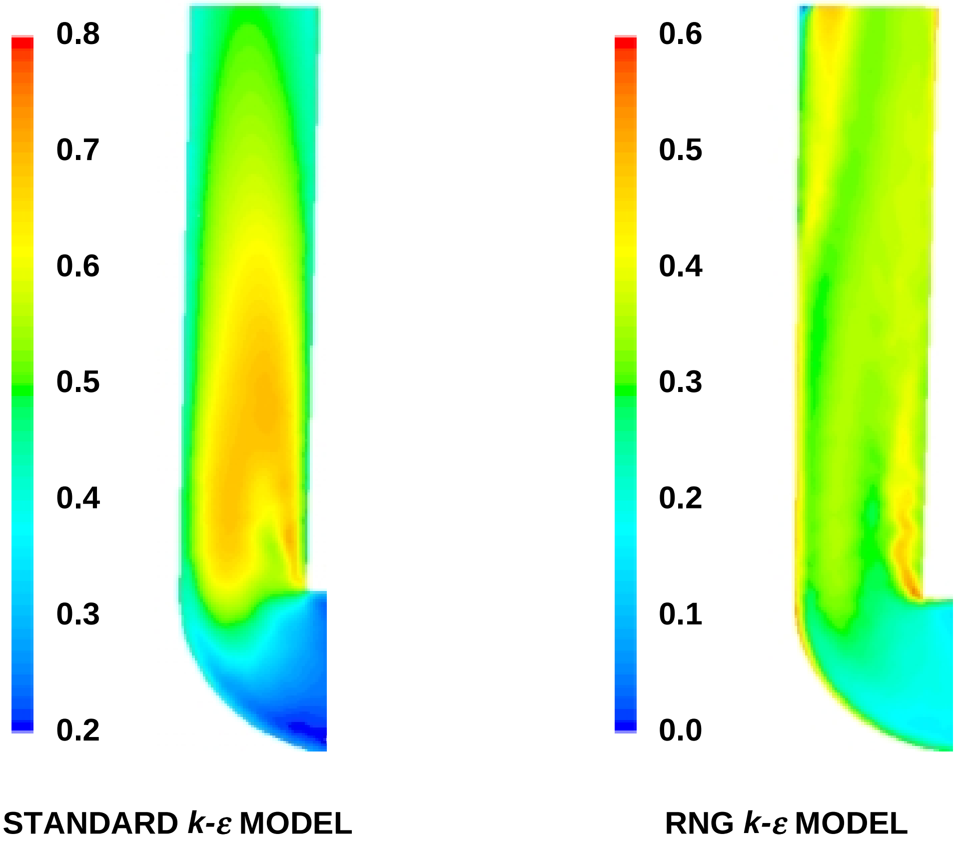

STANDARD k-ε MODEL

RNG k-ε MODEL

Fig. 6 Contour plots of the predicted turbulence intensity in the annular passage following the swirl vanes for both turbulence models. The contour plots correspond to the periodic boundaries at $\theta = 0^{o}$ and $\theta = 30^{o}$, and the scale ranges from 0.2 - 0.8 for the standard k-ε model and 0 - 0.6 for the RNG k-ε model.

Comparison of predictions and experiment

Figure 7 presents values of the alignment parameter computed from experimental data obtained at the outlet of the annular region following the swirl vanes. The data correspond to various values of the probe angle ranging from 45° to 60° measured from vertical; however, the values of Ψ at a particular radial coordinate are fairly consistent. Near the inner wall, the alignment parameter becomes very large. It was not possible to align the probe in the direction of the flow in this region due to the presence of a recirculation zone; therefore, velocity measurements were not made in this region. The combustion air flows mainly near the outer wall, however, and the inability to measure the velocity in the recirculation zone is not considered significant .

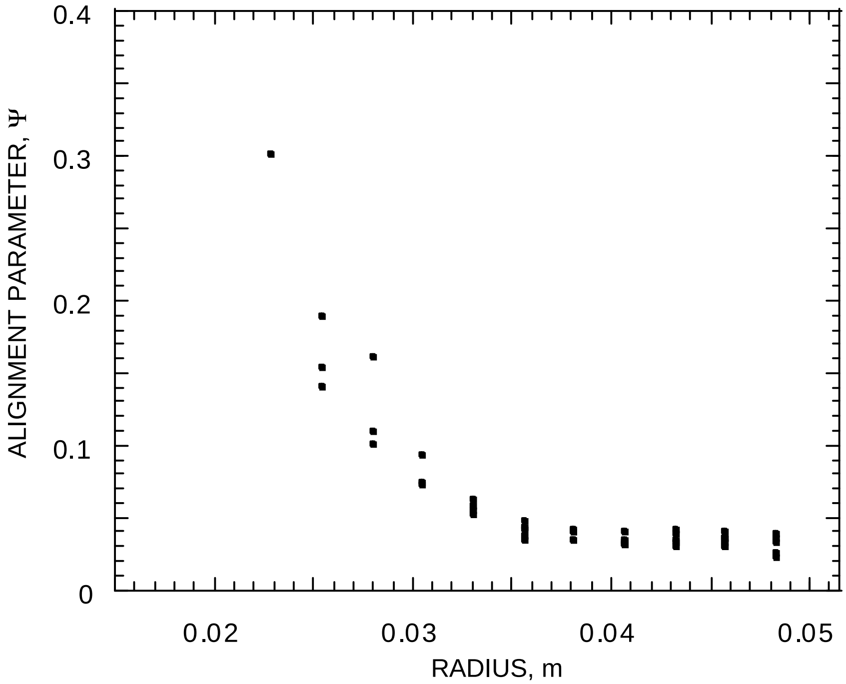

Fig. 7 Variation of the alignment parameter, Ψ, with radial position computed from the experimental data collected at the outlet of the annulus.

The predicted radial profiles of the velocity magnitude at the outlet of the annulus are presented in Fig. 8. Note that the location of the inner and outer walls are r = 0.0175 m and r = 0.0508 m, respectively. Experimental data obtained with the pitot probe are also shown for comparison. The RNG k-ε model compares well with the data, while the standard k-ε model fails to predict the recirculation zone observed near the inner wall of the annulus. The recirculation zone is more apparent in Fig. 9 where the axial and tangential components of velocity computed with the RNG k-ε turbulence model are presented. The radial velocity is negligible and is not shown. Near the inner wall the tangential velocity is essentially zero, while the axial velocity is negative. It is this recirculation zone that stabilizes the flame by transporting fuel vapors from the evaporating spray toward the reaction zone. Thermal energy is also transported by the recirculation zone in the form of combustion products, thus contributing to flame stability. It is therefore imperative that predictive techniques capture this behavior if they are to be used successfully for the design and optimization of these processes.

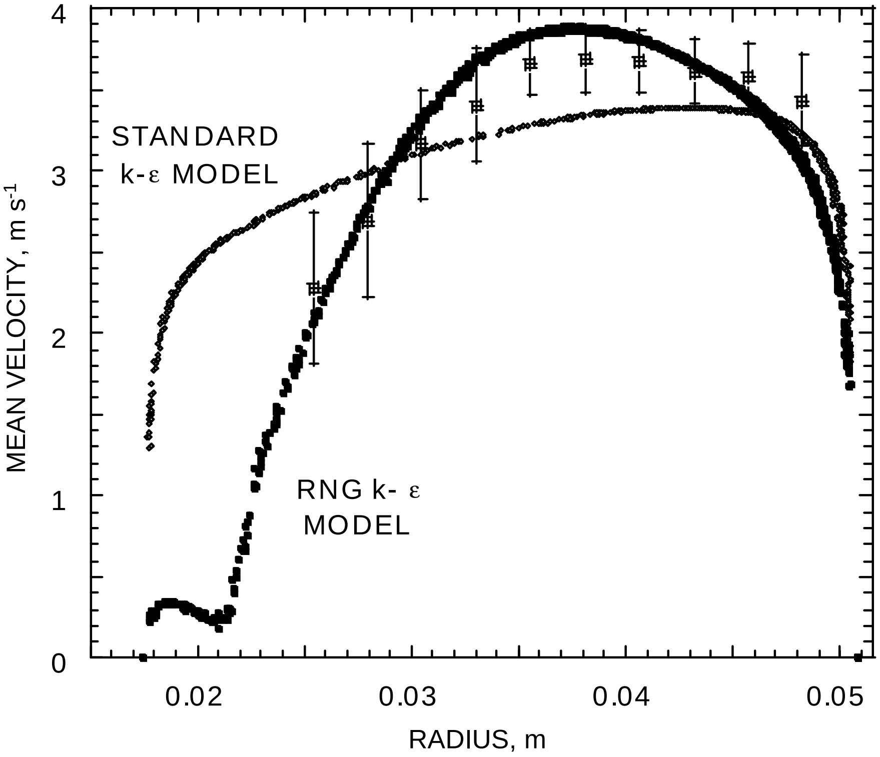

Fig. 8 A comparison of the total velocity profile at the annulus outlet predicted from the numerical simulation using the standard and RNG *k-ε* turbulence models and the experimental data.

The error bars in Fig. 8 correspond to expanded standard uncertainties with a coverage factor of 2 (≈ 95 % confidence interval if the measurements are assumed to be normally distributed about the true mean). The procedure of Taylor and Kuyatt (1994) was used in computing the uncertainty in the experimental measurement. Uncertainties are classified as Type A or Type B, and it is assumed that the combined variance is the sum of the component variances. The Type A variance is a straightforward calculation based upon standard statistical practices applied to repeated measurements. The Type B uncertainties, which can not be quantified from replicated measurements, were estimated using the alignment parameters calculated for the data obtained in the NIST wind tunnel and at the annulus outlet. Variations in Ψ with position and velocity were considered, and data with unacceptably high values of Ψ were discarded. For this reason, data close to the recirculation zone have not been reported.

The radial profiles of the turbulent kinetic energy, *k*, and its dissipation rate, *ε*, at the outlet of the annulus are presented in Fig. 10. These results were obtained with the RNG *k-ε* turbulence model. The turbulent kinetic energy is relatively low in the recirculation zone, but increases abruptly in the region of high velocity gradients at r ≈ 0.023 m. Note that the dissipation rate, ε, is given on a log scale and varies by six orders of magnitude. The relative turbulence intensity varies from ≈ 35 % to ≈ 45 % over the majority of the annulus outlet, with lower values in the recirculation zone. Recall that the outlet of the simulation domain corresponds to the combustion air inlet for the spray combustion reactor (see Fig. 1); therefore, the results presented in Figs. 9 and 10 provide detailed reactor inlet conditions for the velocity components and turbulence parameters, k and ε, when simulating the spray combustion process within the reactor.

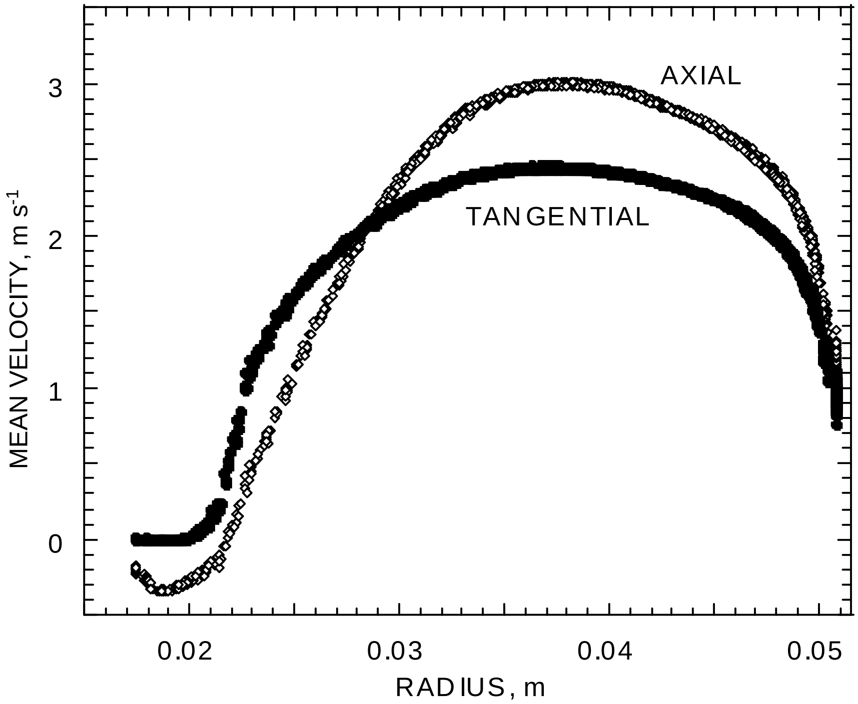

Fig. 9 The axial and tangential velocity profiles at the annulus outlet predicted from the numerical simulation using the RNG k-ε turbulence model.

Swirl number, S

The degree of swirl present in the combustion air entering a burner or furnace has a strong effect on the structure and stability of the flame, and it is therefore an important parameter in the design and optimization of such systems. Despite the importance of characterizing the swirling flow, several obstacles prevent the reliable prediction of highly swirling flow fields. As discussed above, one difficulty encountered when designing these systems is the questionable accuracy of current turbulence models for highly strained flows. This uncertainty results in flow field predictions that are suspect until validated with experimental data. In addition, geometrical and empirical correlations available in the literature are highly geometry dependent and often involve simplifying assumptions (e.g., inviscid flow) that lead to large uncertainties in the predictions.

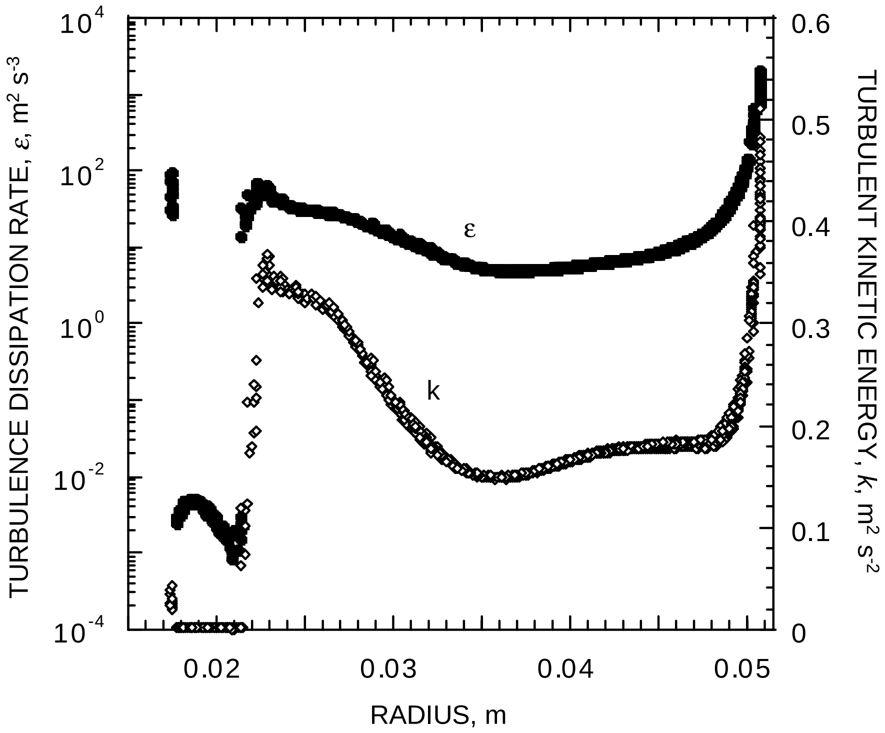

Fig. 10 Turbulent kinetic energy, *k*, and the turbulence dissipation rate, *ε*, at the annulus outlet predicted from the numerical simulation using the RNG *k*-*ε* turbulence model.

Beér and Chigier (1974) present a correlation for predicting the swirl number, *S*, obtained using vane-cascade swirlers, such as the one used here. The swirl number is a non-dimensional parameter that characterizes the degree of swirl present in the flow. It is defined as (Gupta *et al.*, 1984)

$$S = \frac{G_\theta}{LG_z} \tag{12}$$

where L is a characteristic length, typically chosen to be the exit radius of the burner. The terms G_θ and G_z are the axial flux of angular momentum and the axial flux of axial momentum, respectively, and are given by

$$G_\theta = \int_0^\infty \rho u_z u_\theta r^2 dr \tag{13}$$

and

$$G_z = \int_0^\infty (\rho u_z{}^2 + p) r dr \ . \tag{14}$$

Here u_z and u_θ are the axial and tangential velocity components, respectively. For the 12-vane swirl generator investigated in the present study, the characteristic length used was radial coordinate of the outer wall of the annulus (see Fig. 1A), $L = R_0 = 50.8$ mm.

The correlation presented by Beér and Chigier is based upon geometrical considerations and involves a number of simplifications. Assumptions made in the derivation of the correlation include inviscid flow, a uniform axial velocity distribution, and negligible angular momentum losses through the annular region following the vanes. Note that the pressure term in the denominator of Eq. (12) is neglected. With these constraints, the swirl intensity can be predicted from

$$S = \frac{\sigma R_0}{2B}\left[1 - \left(\frac{R_i}{R_0}\right)^2\right], \tag{15}$$

where

$$\sigma = \frac{\tan(\alpha')}{(1 - \mathrm{X})[1 + \tan(\alpha')\tan(\pi / n_v)]}, \tag{16}$$

and

$$\mathrm{X} = \frac{n_v \lambda}{2\pi R_v \cos(\alpha')}. \tag{17}$$

Here, B is the vane height, λ is the vane thickness, n_v is the number of vanes, α' is the vane angle, and R_v is the distance from the burner axis to the vanes. A prime is used to denote the vane angle defined by Beér and Chigier, α', and to differentiate it from the vane angle, α, defined in Fig. 2B. Figure 11 shows the relation between α' and α. The angle α is measured from the center of the vane as shown in Fig. 2B, while α' is measured from the edge of the vane. In the above equations, σ is the ratio of the average tangential and radial velocity components exiting the vanes, and X is a blockage factor that accounts for the thickness of the vanes.

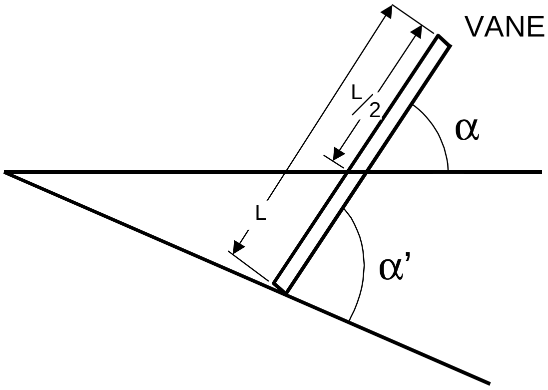

Fig. 11 Relationship between the vane angle, α, and the vane angle as defined by Beér and Chigier, α'.

Using Eqs. (15) - (17), the calculated swirl number for the swirl generator considered here ($\alpha = 50^o$, $\alpha' = 70.7^o$) is $S = 1.0$. The value of the swirl number determined from Eqs. (12) - (14) and the results of the numerical simulation (RNG k-ε turbulence model) is $S = 0.49$. Each of the assumptions presented above will lead to a geometrical correlation that overpredicts the swirl intensity. In addition, a comparison between experimental data and the correlation, Eqs. (15) - (17), shows that the swirl intensity is overpredicted by the correlation, and the discrepancy between the theory and data increases with increasing values of σ (see Fig. 5.4 in Beér and Chigier, 1974). The experimental data presented do not contain values of σ larger than 1.5, while the value of σ computed for the swirl generator used in this study is 2.1; thus, one would expect the actual value of S to be considerably less than that predicted by the correlation, as is the case here.

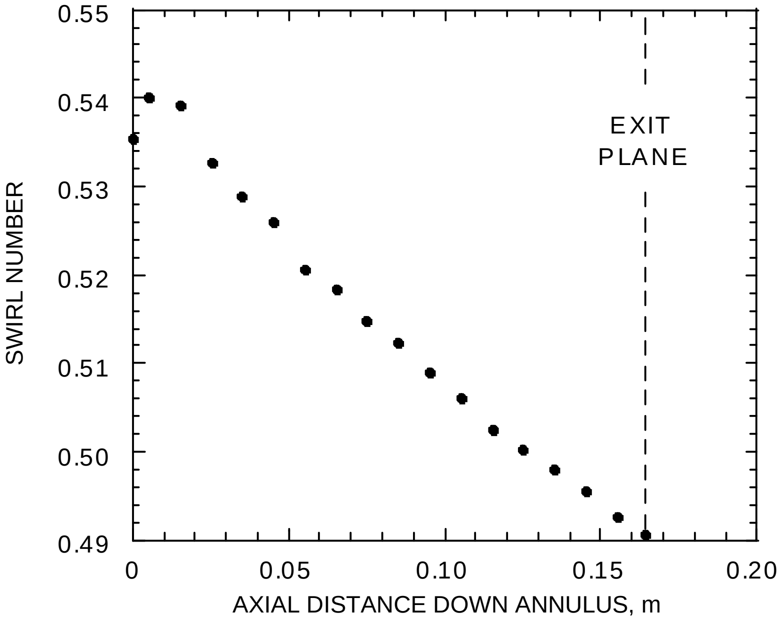

Fig. 12 Variation of the swirl number in the annulus with axial position. The swirl number was calculated from the simulation using the RNG k-ε turbulence model.

Equations (15) - (17) predict the swirl intensity immediately following the vanes, and therefore neglect the decay of angular momentum that occurs in the annular passage downstream of the swirl vanes. The effect of neglecting angular momentum losses can be explored using the numerical simulation by evaluating S at various axial locations in the annulus. Figure 12 presents the computed values of the swirl number in the passage. The swirl intensity of the air entering the annulus immediately downstream of the vanes is approximately $S = 0.54$, and it is reduced to $S = 0.49$ by the exit of the annulus. While the swirl number is reduced due to the angular momentum losses in the annular passage, it does not appear to be the dominant reason that the geometrical correlation overpredicts the exiting swirl intensity for this configuration.

The swirl number, *S*, has been shown to be an important similarity variable for *geometrically similar* swirl generators (Beér and Chigier, 1974; Gupta *et al*., 1984). However, it should be used with caution when comparing the swirl intensity produced by different types of swirl generators. There is some ambiguity due to the choice of a characteristic length in Eq. (12), and *S* is often calculated neglecting the pressure term in Eq. (14), which can result in much higher values of *S*. It is therefore prudent to use care when designing or optimizing processes based upon swirl number correlations.

5. Conclusions

The air flow through a vane-cascade swirl generator was investigated both experimentally and computationally. The experiments reveal a recirculation region near the inner wall at the outlet of the annulus, and this region is predicted using the RNG k-ε turbulence model. The standard k-ε turbulence model is unable to predict the recirculation region for this flow field, and results in overly dispersive velocity and turbulence predictions. Previous investigators have reported superior performance for the RNG k-ε model over the standard k-ε model for highly strained flows, and the results of this investigation provide further validation for this turbulence model for confined, swirling flows.

The simulation incorporating the RNG k-ε model results in a swirl number, *S*, of 0.49 exiting the annular region following the swirl vanes. A geometrical correlation from the literature overpredicts the swirl intensity by a factor of two, and the likely causes have been discussed. In addition, the inlet condition for the combustion air corresponding to the baseline case of NIST's benchmark database for the validation of multiphase combustion models has been characterized. Readers interested in obtaining electronic files of the data presented herein should contact Cary Presser (e-mail: *cpresser@nist.gov*).

6. Acknowledgements

The authors would like to thank Pedro Espina and Lanre Oshinowo for their assistance with the computational aspects of this research, Mike Hall for his help with the wind tunnel measurements, and Mike Carrier for technical support. One of the authors (JFW) wishes to acknowledge the financial support of the NRC/NIST Postdoctoral Research Program. The helpful comments of Francine Battaglia and Tim Johnson concerning this manuscript are also acknowledged.

7. References

Beér, J. M., and Chigier, N. A. (1974). *Combustion Aerodynamics*, Applied Science, London.

Benim, A. C. (1990). Finite Element Analysis of Confined Turbulent Swirling Flows. *International Journal of Numerical Methods in Fluids*. **11**:697-717.

Bird, R. B., Stewart, W. E., and Lightfoot, E. N. (1960). *Transport Phenomena*, John Wiley & Sons, New York.

Fluent 5 User's Guide. (1998). Fluent Incorporated, Lebanon, NH 03766 USA.

Gupta, A. K., Lilley, D. G., and Syred, N. (1984). *Swirl Flows*, Abacus Press, Kent.

Hinze, J. O. (1975). *Turbulence*, McGraw-Hill Publishing Co., New York.

Issa, R. I. (1986). Solution of Implicitly Discretized Fluid Flow Equations by Operator Splitting. *Journal of Computational Physics*. **62**:40-65.

Jaw, S. Y., and Chen, C. J. (1998). Present Status of Second-Order Closure Turbulence Models. I: Overview. *Journal of Engineering Mechanics*. **124**:485-501.

Kreith, F. (1958). *Principles of Heat Transfer*, International Textbook Company, Scranton, pp. 277-283.

Launder, B. E., and Spalding, D. B. (1972). *Lectures in Mathematical Models of Turbulence*, Academic Press, London.

Launder, B. E., and Spalding, D. B. (1974). The Numerical Computation of Turbulent Flows. *Computer Methods in Applied Mechanics and Engineering*. **3**:269-289.

Lien, F. S., and Leschziner, M. A. (1994). Assessment of Turbulence-Transport Models Including Non-Linear RNG Eddy-Viscosity Formulation and Second-Moment Closure for Flow Over a Backward-Facing Step. *Computers in Fluids*. **23**:983-1004.

Papageorgakis, G. C., and Assanis, D. N. (1999). Comparison of Linear and Nonlinear RNG-Based k-ε Models for Incompressible Turbulent Flows. *Numerical Heat Transfer, Part B*. **35**:1-22.

Sheen, H. J., Chen, W. J., and Wu, J. S. (1997). Flow Patterns for an Annular Flow Over an Axisymmetric Sudden Expansion. *Journal of Fluid Mechanics*. **350**:177-188.

Shyy, W., Thakur, S. S., Ouyang, H., Liu, J., and Blosch, E. (1997). *Computational Techniques for Complex Transport Phenomena*. pp. 163-230. Cambridge University Press, Cambridge, UK.

Smith, L. M., and Reynolds, W. C. (1992). On the Yakhot-Orszag Renormalization Group Method for Deriving Turbulence Statistics and Models. *Physics of Fluids A*, **4**:364-390.

Taylor, B. N., and Kuyatt, C. E. (1994). *Guidelines for Evaluating and Expressing the Uncertainty of NIST Measurement Results*. NIST Technical Note 1297, 1994 Edition.

Widmann, J. F., Charagundla, S. R., Presser, C., & Heckert, A. (1999). Benchmark Experimental Database for Multiphase Combustion Model Input and Validation: Baseline Case. NISTIR 6286. National Institute of Standards and Technology, Gaithersburg, MD 20899-8360, USA.

Yakhot, V., and Orszag, S. A. (1986). Renormalization Group Analysis of Turbulence: I. Basic Theory. *J. Scientific Computing*, **1**:1-51.

Yakhot, V., Orszag, S. A., Thangam, S., Gatski, T. B., and Speziale, C. G. (1992). Development of Turbulence Models for Shear Flows by a Double Expansion Technique. Physics of Fluids A. **4**:1510-1520.

Yakhot, V., and Smith L. M. (1992). The Renormalization Group, the ε-Expansion and the Derivation of Turbulence Models. *Journal of Scientific Computing*. **7**:35-61.

Yin, M., Shi, F., and Xu, Z. (1996). Renormalization Group Based k-ε Turbulence Model for Flows in a Duct with Strong Curvature. *International Journal of Engineering Science*. **34**:243-248.